

X-68 Velociraptor: A Theoretical Design of a Hydrogen Scramjet-Integrated Hypersonic Vehicle

K. Koenig, M. Nanni, M. Ruggeri, R. Patel, A. Rindani, and W. Greder
School of Astronautics and Aeronautics, Purdue University

A theoretical design for NASA’s next experimental vehicle, the X-68 Velociraptor, is reported. The X-68 is a hypersonic vehicle powered by a hydrogen-fueled scramjet engine. While scramjet engines have been tested on the ground in wind tunnels and direct-connect test rigs for decades, few have been tested in flight. This work details the full design and mission plan of a new hypersonic vehicle concept targeted at collecting more experimental flight data, including trajectory planning, propulsion cycle analysis, scramjet engine development, thermal management, and the overall mechanical design of the vehicle. The vehicle is optimized for a cruise altitude of 104,843 feet at a freestream Mach number of 9. It has an estimated propelled range of 723 miles, with an additional glide range of 792 miles during the descent.

1 Introduction

Hypersonic scramjet-integrated vehicles offer promising new capabilities for high-speed flight, achieving high specific impulse at flight Mach numbers greater than 5 [1]. However, they present many unique challenges: stringent thermal management and structural requirements as well as achieving effective flow deceleration and supersonic combustion make designing a scramjet vehicle no simple task. Individual scramjet components have been tested in lab settings in direct-connect and free jet wind tunnels since the 1950s, but no scramjet vehicle flew until the early 1990s [2].

Since then, the US has publicly flown multiple scramjet vehicles, notably NASA’s X-43 Hyper-X and Boeing’s X-51 Waverider. This paper presents the design for NASA’s next scramjet vehicle: the X-68 Velociraptor. Due to design and mission constraints, the X-68 must 1) use hydrogen for fuel, 2) operate in a fully scramjet combustion mode 3) be manufactured from existing materials, 4) have a range greater than 500 miles, 5) weigh less than 4000 lbf at take-off, and 6) be launched from a B-52 Stratofortress. All these requirements are met or exceeded, and the full detailed design of the vehicle and mission plan is presented.

2 Methodology

2.1 Trajectory

For this test flight, a B-52 is used to lift the vehicle and booster to 40,000 ft at Mach 0.7. The vehicle starts its propelled phase at Mach 5 and 78,000 feet. After investigation, it was found that a suitable booster for this task is SpaceX’s Falcon 1, which uses a Merlin 1 liquid rocket engine. After the boosted phase, the scramjet engine is ignited and powers the vehicle through a constant angle of attack (θ) trajectory to an altitude of 104,843 ft and a speed of Mach 9. The vehicle then begins a cruise trajectory at a constant Mach number of 9 and an altitude that balances the lift and weight forces at $\theta = 0$. After burning through all of its propellant, the vehicle glides to the ground.

The boosted part of the trajectory is governed by the nine equations of a constant-q trajectory [2]. The first part of the trajectory assumes a linear acceleration up to the desired dynamic pressure of 1,086 lb/ft². An acceleration time of 15 seconds was chosen, as this is the smallest time that satisfies the maximum thrust of the booster. The Falcon 1 is able to produce a maximum thrust of 102,000 lbf with a specific impulse of 255 s and a weight of 26,455 lbf. This gives an initial total of 30,455 lbf when the booster-vehicle system is launched from the B-52. The booster-vehicle system is connected to the aircraft with impact failure bolts [3]. These are usually used for space purposes, as they reduce the shock on the structure and do not produce fragments, decreasing the risk of damaging structures. These same devices are also used to separate the booster from the scramjet.

For the propelled trajectory of the X-68, it was assumed that the vehicle consumes 2.2 lbf/s of fuel during the constant Mach number trajectory and between 0.44 and 2.2 lbf/s while climbing, increasing linearly with flight Mach number. The climb begins with $\theta = 2^\circ$ up to Mach 8 and then it linearly decreases to 0° when it reaches Mach 9. For the aerodynamic coefficients of the vehicle, the same coefficients as the X-43 were used, given that the X-68’s shape is similar. From the work of Navó and Bergara [4], $c_D = 0.0271$ and $c_L = 0.0899$ were used. For the estimation of the altitude required for a constant Mach number and balanced flight at $\theta = 0^\circ$, equilibrium equations along the x and z axis of the vehicle with zero acceleration were used. This analysis was first used to estimate the starting condition for the scramjet, and then continuously through the cruise while updating mass to estimate the altitude of the constant Mach number trajectory. The vehicle starts with an initial weight of 4,000 lbf and finishes with 2,866 lbf after burning all the fuel.

2.2 Propulsion Cycle

The propulsion cycle brings together the separate components designed individually and a cycle analysis serves to provide a holistic view of the X-68 engine. The cycle is

divided into three distinct parts viz. compression, combustion, and expansion. The inlet-isolator system serves to provide compression, the combustor the combustion, and the nozzle the expansion.

Time histories of static temperature, static pressure, specific heat at constant pressure (c_p), amount of heat release (\dot{Q}), and specific heat ratio (γ) were obtained from the combustor and the inlet-isolator system (heat release for which is zero).

The non-dimensional entropy ($\frac{s-s_\phi}{c_p}$) was plotted against the non-dimensional static temperature (normalized with the ambient temperature T_ϕ ; $\frac{T}{T_\phi}$) using the equation given below [2]

$$\frac{s-s_\phi}{c_p} = \ln \frac{T}{T_\phi} - \frac{\gamma-1}{\gamma} \ln \frac{P}{P_\phi} \quad (1)$$

where T_ϕ and P_ϕ are the static temperature and pressure at ambient conditions. In this case, the ambient conditions are taken at an altitude of 105,000 ft and the cruise is at Mach 9. The inlet-isolator geometry was set to give a compression ratio of 250 and a fuel-flow rate of 2.2 lbm/s were taken as nominal values while obtaining the non-dimensional T-s diagram.

In addition, a parametric analysis with varying fuel flow rates and varying compression ratios with a fixed air mass flow rate, hence in effect varying fuel-air ratios was carried out. The analysis consisted of observing the cycle efficiency (η_0) and specific thrust.

The fuel flow rates were varied from 0.66 lbm/s to 3.96 lbm/s and compression ratios from 120 to 250 with the air mass flow rate being fixed at 39.0 lbm/s. These values encompass the flow rates that were actually realized during the cruise phase of the flight. The nozzle was assumed to operate at an efficiency of 0.98 with an exit design Mach number of 3.8, and the combustor analysis was performed at an efficiency of 0.8. Cycle efficiency and performance equations are as follows:

$$f = \frac{\eta_b \dot{m}_f}{\dot{m}_{air}} \quad (2)$$

$$\nu = \frac{u_\phi}{u_9} \quad (3)$$

$$\eta_p = \frac{2\nu(f+1-\nu)}{2\nu(f+1-\nu) + (f+1)(1-\nu^2)} \quad (4)$$

$$\eta_{th} = \frac{\dot{Q}}{\dot{m}_f h_{pr}} \quad (5)$$

$$\eta_0 = \eta_p \eta_{th} \quad (6)$$

$$T_{sp} = (1+f)u_9 - u_\phi \quad (7)$$

where f represents the effective fuel-air ratio, ν represents the velocity ratio, η_b is the burner or combustor efficiency, η_p is the power efficiency, η_{th} is the thermal efficiency, u_ϕ is the free-stream air velocity, u_9 is the velocity at the nozzle and h_{pr} is the calorific heating value of hydrogen.

2.3 Inlet

For hypersonic inlets, the shocks that come off of the inlet are the key defining feature of the design methodology. These shock angles (β) can be determined using the starting Mach (M_1) and the turning angle (θ) with Equation 8.

$$\tan \theta = 2 \cot \beta \frac{M_1^2 \sin^2 \beta - 1}{M_1^2 (\gamma + \cos^2 2\beta + 2)} \quad (8)$$

where position 1 indicates the state before the shock. For this case, γ is assumed to be a constant 1.4 for air.

There are three primary design methods used to utilize these oblique shocks to compress and slow the air for combustion: external, internal, and mixed compression inlets. The book *Hypersonic Propulsion* by Heiser and Pratt [2] and Michael Smart's article [5] give visuals and a more detailed description of the benefits and drawbacks of each design.

As discussed in Section 2.1, the vehicle will be launched first off of a B-52 and then boosted to Mach 5. By starting at a higher velocity, the inlet can avoid many of the issues created when trying to start at low Mach numbers. Based on this, the mixed compression inlet is the best option out of the three due to increased performance. While this design is often longer than the internal or external options, by integrating this design directly into the underbody of the airframe, similar to the X-43 design [2], the impact of this drawback can be reduced.

A case study completed using Smart's article [5] and the X-43 design [6] confirmed the use of the mixed inlet. While this case study does not determine that the mixed inlet is the best choice, it does prove that the design characteristics are viable for real-life inlet systems.

Three major considerations had to be met by the inlet design. First, the inlet should be operable for values other than just the cruise condition. This is the most broad consideration and is met by choosing the correct design methodology as a whole instead of a specific mechanical choice.

Secondly, the total pressure recovery must be greater than the requirement set by the MIL-E-5007D [7]. This value is set by the equation given on page 13 of the form. With the cruise Mach of 9 as set by the trajectory, the total pressure recovery must be greater than 0.1067.

Lastly, the inlet must work in conjunction with the isolator to create the properties necessary for hydrogen combustion. These requirements are set by the combustion dynamics that are discussed further in section 2.5.

Based on these considerations, the design chosen was sourced from Torrez's conference paper [8]. This design was developed to gain better performance at off-design conditions without mechanical actuation on flight. Computational Fluid Dynamics were used to analyze the model. This analysis shows an increase in performance at all points other than the design conditions, where it saw only marginal decreases.

This design differentiates from the normal on-design inlet

design by considering differing flight conditions for different sections of the inlet. It also includes a shoulder that stops shocks from progressing upstream at lower Mach numbers.

The paper includes an algorithm for iteratively solving for the inlet geometry using a selected pressure increase, a range of Mach values, and flexibility in terms of the number of internal and external flow turns.

Much of the algorithm is described in the Torrez paper but the algorithm was slightly altered due to differences in the iteration methods and simplifications to the theta-beta-mach equation that were made in the Torrez paper.[8] For developing design points, the initial conditions were all taken from the source except for the height between the initial points was set to one to allow for easier intuition regarding the length of the system. The last turn within the cowl was also simplified with a set flow path length before the turn because the equations presented in the Torrez are under-constrained. This is very similar to the work done in the Medina article when faced with the same problem. The rest of the equations were revised using basic geometric relations [9].

This algorithm was then implemented into a MATLAB code. This code and algorithm were verified using the conditions and results presented on pages 6 and 7 of the Torrez paper. Table 1 shows the error between the calculated values for the design algorithm and the values presented in Torrez [8].

	i	x_{Calc}	z_{Calc}	x_{Tor}	z_{Tor}	% Err	% Err
r	1	0	0	0	0	0.00	0.00
	2	3.257	0.234	3.192	0.238	2.04	1.78
	3	4.764	0.468	4.706	0.483	1.23	3.15
	4	6.699	0.976	6.570	0.978	1.97	0.26
	5	6.817	0.993	6.704	0.997	1.68	0.44
c	1	6.077	1	5.991	1	1.44	0.00
	2	6.325	1.036	6.410	1.059	1.34	2.18

Table 1: Comparison of Torrez

The max error between Torrez and the calculated values obtained from the revised code is only 3%. A majority of the points have percent errors at or less than 2%. This certifies the accuracy of the design code.

In addition to the comparison to the source material work, Medina compared the results of Torrez's code to real-life systems like the X-51 and X-43 [9]. The results show that all open-source values of the X-43 matched closely with the outputs of the Torrez algorithm.

2.4 Isolator

The isolator is much harder to model with a simple mathematical equation. Equation 9 that was used is from a paper from Waltrup and Billig that took data from Mach 1.5 to 2.7 [2]. While the X-68's entrance Mach values are often outside this range, it is a good starting point for the isolator design.

$$\frac{L_t}{D} = \frac{\sqrt{\frac{\theta_1}{D}}}{(M_1^2 - 1) R_\theta^{0.25}} \left[50 \left(\frac{P_2}{P_1} - 1 \right) + 170 \left(\frac{P_2}{P_1} - 1 \right)^2 \right] \quad (9)$$

where θ is the boundary layer momentum thickness, R_e is the Reynolds number. Position 1 indicates the flow entering the isolator and position 2 indicates the exit. Because the pressure rise is completed with the inlet system the more important factor of the isolator is its ability to slow down the flow. Based on the literature of hydrogen-burning scramjet combustion operations, the flow should be at or below Mach 2.8. Therefore Mach after the isolator is solved with Equation 10b.

$$X = \frac{\left(1 + \gamma M_1^2 - \frac{P_2}{P_1} \right)^2}{M_1^2 \gamma^2 \left(1 + \frac{\gamma-1}{2} M_1^2 \right)} \quad (10a)$$

$$M_2 = \sqrt{\frac{X}{1 - X \left(\frac{\gamma-1}{2} \right)}} \quad (10b)$$

The length and Mach can be solved over a range of pressure ratios. These tables can be extrapolated to determine the length-to-height ratio for a given Mach.

Computational fluid dynamics modeling should be used in future models to determine the necessary length. This would give a much more accurate model of the combustor input as well. The above equations are both exponential so a small change in length has a massive impact on the flow.

2.5 Combustor

The combustor increases the total enthalpy of the engine's bulk flow so that this excess enthalpy can then be converted into thrust in the nozzle. This is accomplished by injecting fuel into the engine and combusting it with the bulk airflow, releasing heat. Since scramjet combustion is supersonic, these fuel injection and combustion processes further complicate realizing the necessary heat release [1]. To achieve the required heat release, the X-68's combustor features four main sections: initial upstream normal port injectors, ramp hypermixers, a cavity flameholder, and a final diverging duct. These sections are designed such that 1) the fuel becomes adequately premixed to facilitate high heat release, and 2) the combustion is stable to avoid flameout.

2.5.1 Combustor Component Modeling

The main function of the initial upstream normal port injectors are to begin premixing fuel into the bulk flow prior to the main combustion region. Since the fuel is injected normal to the bulk flow, the jet penetration depth governs the overall mixing of the fuel and air. Segal offers a correlation to calculate jet penetration depth into high-Mach number air flows [1]:

$$\frac{y}{D} = A \left(\frac{q_f}{q_a} \right)^B \left(\frac{x}{D} + C \right)^E \left(\frac{\delta}{D} \right)^F \left(\frac{MW_f}{MW_a} \right)^G \quad (11)$$

where y is jet penetration depth, D is port diameter, q_f and q_a are the dynamic pressures of the fuel and air, x is

axial distance, δ is boundary layer thickness, and MW_f and MW_a are the molecular weights of the fuel and air. A , B , C , E , F , and G are coefficients that vary based on the air Mach number and are shown in Appendix A.

The mixing efficiency is then used to quantify the overall level of mixing between the fuel and air. It is defined as the ratio of the amount of fuel that would react in a partially-mixed flow to the amount that would react in a fully uniform mixture [2]. An empirical relation for the mixing efficiency of hydrogen injected normal to an air crossflow was used to determine the mixing efficiency through the first section [2]:

$$\eta_{M,normal} = \left\{ \frac{x}{L_m} + \frac{1}{50 + 1000\alpha} \right\}^\alpha \quad (12)$$

$$\frac{L_m}{b} = 0.179C_m e^{1.72\phi_0} \quad (13)$$

where η_M is mixing efficiency for the normal ports, L_m is mixant depletion length, x is axial distance, α is a fit parameter, b is the sum of the entry scales of segregation, C_m is the mixing constant, and ϕ_0 is the global equivalence ratio. α was taken to be 0.25, since the injectors are closely spaced. b was taken as half the duct height, as the combustor is symmetric. The mixing constant varies between 25 and 60, and was taken as 25 due to the strong penetration depth that would lead to a shorter depletion length.

The ramp hypermixers serve to inject more fuel into the bulk flow and further enhance fuel-air mixing. As flow passes through the oblique shock anchored at the ramp base and spills over the sides of the ramp, axial vortices are generated [2]. This greatly enhances the mixing efficiency, which is calculated using Equation 14 [2]:

$$\eta_{M,ramp} = \frac{1 - e^{-Ax/L_m}}{1 - e^{-A}} \quad (14)$$

where A is a fit parameter. Studies have shown that swept ramps have higher mixing efficiencies than unswept ramps, and so the ramps chosen have a 15° sweep angle. For this geometry and the high freestream Mach number, a suitable value for A is 4.9.

Because the ramps inject fuel parallel to the bulk flow, mixing is governed by the mixing layer growth of the fuel into the air. Dimotakis gives a correlation for the mixing layer growth between turbulent shearing gases, accounting for attenuation due to compressibility effects [2]:

$$\frac{\delta_m}{x} = 0.49 * f(M_c) * C_\delta \left(\frac{1-r}{1+s^{1/2}r} \right) \left(\frac{1+s^{1/2}}{2} \right) \times \left\{ 1 - \frac{(1-s^{1/2})/(1+s^{1/2})}{1+1.29(1+r)/(1-r)} \right\} \quad (15)$$

$$f(M_c) = 0.2 + 0.8e^{-3M_c^2} \quad (16)$$

where δ_m is mixing layer height, M_c is convective Mach number, C_δ is a growth constant, and r and s are the velocity and density ratios of the gases. C_δ varies from 0.25 to

0.45, and was taken as 0.45 since the swept ramp's vortices will maximize the mixing layer growth.

The cavity flameholder stabilizes the engine's combustion, preventing flameout at high freestream Mach numbers. The cavity's recirculation zone entrains hot combustion products, increasing particle residence time and feeding the main combustion reaction. The cavity flame is piloted by injecting a small amount of fuel at the backwards-facing step.

In a study by Song et al., it was seen that the mixing efficiency for a fuel-lean, base-fed cavity with an array of small injectors varies in a linear fashion from roughly 15% to 60% over the length of the cavity [10]. Since the X-68's combustor has a similar geometry and injectors to this study, the cavity mixing efficiency model was approximated as such, where L_{cavity} is the cavity length:

$$\eta_{M,cavity} = 0.15 + \frac{0.6 - 0.15}{L_{cavity}}x \quad (17)$$

The diverging duct gives the flow more time to react and release heat before exhausting into the nozzle. This increases the combustor's overall combustion efficiency. The length and expansion of this duct was sized based upon reaching a combustion efficiency of 80% without thermally choking the engine. The combustion efficiency used was one based upon temperature rise [2]:

$$\eta_b(x) = \frac{\tilde{T}(x) - T_3}{T_{ad} - T_3} \quad (18)$$

where η_b is combustion efficiency, \tilde{T} is mean static temperature of the bulk flow, T_3 is combustor entrance static temperature, and T_{ad} is the adiabatic flame temperature. This form of η_b was chosen over one based on percentage of fuel burned because it is a better measure of overall heat release that can be used for propulsion [2].

2.5.2 Combustor Aerothermodynamic Model

The combustor was analyzed using the generalized 1-D flow analysis outlined by Shapiro [11]. This method uses a set of ODEs to find the Mach number and static pressure profiles of the bulk flow, given known changes in the flow area, temperature, mass flow rate, ratio of specific heats, and molecular weight. It was assumed that friction losses, heat transfer to the combustor walls, and any work interactions were all negligible. These ODEs are shown in Appendix B.

The ODEs were solved in MATLAB using a discretized 1-D marching scheme with a step of 0.05° . The area schedule was predefined and the fuel addition schedule was determined via mixing efficiency correlations.

The correlations assume a pure air flow at the entrance of each section. However, in reality, each section builds upon one another and the mixing efficiencies compound. To model this, the mixing efficiency was taken as the average between that of the stronger mixing section and the sum of both section's efficiencies. In the ramp section, for example:

$$\eta_{M,tot} = \frac{1}{2} \left(\eta_{M,ramp} + \frac{\eta_{M,ramp} + \eta_{M,normal}}{2} \right) \quad (19)$$

Once the combined mixing efficiency reached 100%, the fuel was considered to be fully premixed.

With a known mixing efficiency profile, the amount of fuel that participated in the reaction at each step was calculated based on the available uncombusted fuel in the flow. This small amount of combusted fuel was then taken as the mass added to the bulk flow over the step.

To find the temperature, γ , specific heat, and molecular weight, NASA's CEA program was called at each step. It is assumed that the fuel only combusts at the fuel-bulk flow shear layer, where the fuel and air are in near-stoichiometric proportions. Calling CEA, the adiabatic flame temperature, γ , specific heat, and molecular weight of the combustion products were computed. Using the fuel addition schedule alongside the stoichiometric fuel-to-air ratio, the total amounts of fuel and air that combusted at each step were determined. The mass and mole fractions of these combustion products and the bulk flow were then calculated, and the properties of the new mixture were updated.

With static temperature and pressure, Mach number, and γ known, the total pressure and temperature were determined with total-to-static relations. This process was then repeated at each step until the full aerothermodynamic property profiles across the combustor were known, as shown in Figure 1.

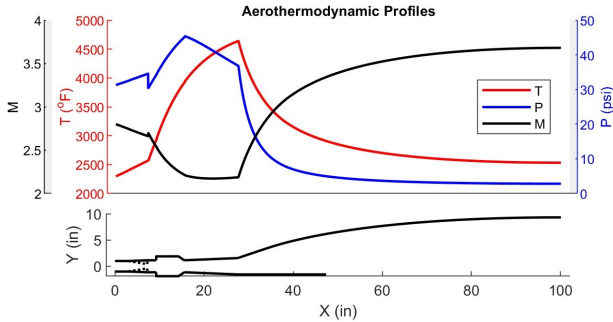


Figure 1: Temperature, pressure, and Mach number profiles through the combustor and nozzle.

2.6 Nozzle

The nozzle takes the increased enthalpy of the flow exiting the combustor and converts it into kinetic energy and thrust. In subsonic combustion engines, this energy conversion is achieved by accelerating the flow to supersonic speeds through a converging-diverging duct. In a scramjet, however, the flow exiting the combustor is supersonic, and so only a diverging duct is required for flow acceleration.

2.6.1 Nozzle Geometry

The contour of the nozzle was determined using the method of characteristics (MOC) for a 2-D, planar, unchoked flow with a sudden expansion at the nozzle's throat [2]. At the design condition, this MOC contour provides perfect axial flow at the nozzle exit, maximizing the thrust efficiency. The sudden expansion at the throat generates a centered

simple Prandtl-Meyer expansion fan, and all the characteristics originate at the nozzle entrance. Because of this, a sudden expansion necessitates the shortest distance to perfectly reflect all the characteristics, resulting in a minimum length nozzle contour, as shown in Figure 1.

In an ideal MOC contour, the characteristics generated at the top and bottom throat corners perfectly reflect one another, resulting in a plane of symmetry. This plane of symmetry can then be replaced by a physical flap that reflects the characteristics in the same manner [2]. This flap only needs to extend out to the intersection point of the final characteristic, as the flow reaches the freestream static pressure along this line. After this point, the flow is bounded by the upper physical expansion surface and the lower pressure boundary. To minimize vehicle size, this expansion surface is also the aft end of the vehicle underbody.

2.6.2 Nozzle Aerothermodynamic Model

The aerothermodynamic property profiles were determined assuming isentropic flow through the nozzle. As can be seen in Figure 1, there is a rapid pressure drop following the sudden expansion at the nozzle throat. This pressure drop freezes the chemical kinetics, resulting in an approximately constant species composition and no further heat release in the nozzle. Assuming the wall heat transfer and friction are negligible, the total temperature and pressure in the nozzle are constant. With the known combustor exit properties and nozzle geometry, the profiles in Figure 1 were then found using the mass flow function, D .

$$D = \frac{M}{(1 + \frac{\gamma-1}{2} M^2)^{\frac{1}{2} \frac{\gamma+1}{\gamma-1}}} \quad (20)$$

$$D_x(M_x) = D_4(M_4) \frac{A_4}{A_x} \quad (21)$$

where A is flow area. Once the mass flow function at each point was known, the Mach number was implicitly solved for, and the static temperature and pressure were calculated using total-to-static relations.

2.7 Thermal Management

In addressing the thermal challenges of the X-68 hypersonic vehicle, the present study focused on developing an efficient cooling system using hydrogen as the coolant. This system initiates at the combustor, proceeds to the nozzle, covers the leading edge, and extends to the inlet and isolator before the hydrogen is injected into the combustion chamber. This solution was inspired by a previous study conducted by Rued, Ebenhoc, and Mark [12].

It was employed an algorithm to calculate the coolant temperature T_c and the temperatures on both sides of the wall of the body (T_{hw} for the hotter side and T_{cw} for the cooler side) at each segment dx along the x-direction. The current analysis is confined to convective and conductive heat transfer, reserving the exploration of radiative heat transfer for future work. The fundamental heat transfer

equations applicable to this system are as follows [13][14]:

$$q_1'' = h_g(T_r - T_{hw}) \quad (22)$$

$$q_2'' = \frac{k_w}{t}(T_{hw} - T_{cw}) \quad (23)$$

$$q_3'' = h_c(T_{cw} - T_c) \quad (24)$$

For the convective heat transfer coefficients, it was first addressed the hot gas side. Utilizing the Bartz correlation [15], this aspect was accurately modeled, accounting for property variations in the hot gas flow. The coefficients h_g and σ are described in Appendix C (equations 32, 33).

The hot gas temperature is notably influenced by viscous dissipation within the compressible boundary layer, leading to enthalpy losses. A correction factor “r” was incorporated to capture this effect, as detailed in equation 25. This factor varies based on flow type, being \sqrt{Pr} for laminar and $Pr^{\frac{1}{3}}$ for turbulent flow [16].

$$T_r = T \left(1 + r \frac{\gamma - 1}{2} M^2 \right) \quad (25)$$

In defining the initial conditions for the hydrogen coolant, a temperature of 40K was selected to avoid discontinuities identified via the “CoolProp” tool in Matlab. The chosen pressure is 20% above the critical pressure, ensuring the hydrogen remains a supercritical fluid throughout the cooling channels, thereby preventing the detrimental “two-phase effect.” The Nusselt number in the coolant channel is given by the Gnielinski correlation, which is the most complete for a tube [14] (see Appendix C equation 34), with the skin friction governed by the von Kármán equation (see Appendix C equation 35). [17].

The correlation between the Nusselt number and the convective heat transfer coefficient h_c is provided by the Dittus-Boelter correlation (see Appendix C equation 36) [13].

Newton’s method was applied to determine the converged wall temperature T_{hw} , combining Equations 22, 23, 24 to formulate $F(T_{hw})$. This converged value of T_{hw} is defined by the condition $F(T_{hw}) = 0$.

$$F(T_{hw}) = T_c - T_{hw} + (T_r - T_{hw}) \left(\frac{t}{k_w} + \frac{1}{h_c} \right) h_g \quad (26)$$

Where h_g depends also on T_{hw} as illustrated in equation 32 (Appendix C). Upon determining T_{hw} , the heat transfer q_1'' could be calculated using Equation 22 and then the coolant temperature T_c for each length increment dx [13] can be determined. The pressure drop in the system is calculated using the Darcy–Weisbach equation (see Appendix C equation 37).

$$T_c = T_c + q_1 \frac{dA}{(m_f C_{pH2})} \quad (27)$$

2.8 Mechanical Design

2.8.1 Tanks

The tank design methodology focused on minimizing dry mass while safely containing cryogenic hydrogen per range and mass requirements. A conservative tank geometry optimization balanced mass versus volumetric efficiency within the vehicle.

Because the scramjet operates with liquid hydrogen fuel stored at 20 K, boil-off was a major design concern. A 1D thermal model was used to estimate propellant boil-off during boost and cruise so that excess could be brought along for the required range. An iterative insulation sizing was conducted with a material based on low thermal conductivity and proven utility to reduce boil-off and temperature gradients. This sizing method inputted insulation thickness to return heat flux, boil-off mass, and insulation weight, and this was manually optimized by checking its constraint on the overall vehicle. The thermal circuit heat flux addition was estimated as:

$$q'' = \frac{T_{amb} - T_{tank}}{t_{insul}/k_{insul} + r \ln(r/L)} \quad (28)$$

From the heat flux and flight times for the boost and cruise sections of the trajectory, the boil-off was determined using the latent heat of vaporization of liquid hydrogen. As this is a steady approximation, a factor of safety of 1.75 was applied to this boil-off mass calculation, ensuring that there would be no fuel limitations to this flight.

Tank volume was determined from the hydrogen mass requirement of 400 kg plus the excess due to boil-off using a fuel density of 70.8 kg/m^3 . A 1D structural analysis was used to size cylindrical tank dimensions based on the hoop and axial stress equations [18] subject to pressure loads, with a safety factor of 1.5 on maximum expected operating pressure (MEOP). The equations are:

$$\sigma_\theta = \frac{Pr}{t}, \sigma_{ax} = \frac{Pr}{2l} \quad (29)$$

By manually setting the tank length based on the overall vehicle size constraints, and pressure based on what was necessary considering losses and entrance pressures to the combustor and cooling channels, the radius and thickness of the tank could be solved. Material selection for the hydrogen tank was based on a literature assessment of materials used in cryogenic applications with the capabilities to withstand the parameters used in the sizing analysis.

A pressurization tank was also considered as a part of the fluid system. This tank was sized for 2900 psi using helium as the working gas. By applying the ideal gas law and using 10% ullage for consideration, the extra volume necessary and the overall amount of helium required could be calculated. The required volume was then used in a similar analysis to the hydrogen tank to determine helium tank dimensions. The fluid system weight and pressure loss for the tanks were estimated using typical components, such as pressure regulators, valves, heat exchangers, and filters

[19]. Figure 18 in Appendix D showcases the general flow through the most integral components of the fluid system.

2.8.2 Vehicle Structure

The vehicle structure sizing considered the dynamic pressure and material properties of available, reliable options. The thickness was determined from equation 29 using a limit of 50% of the maximum yield stress requirement, maximum dynamic pressure, and a general maximum radius based on the component sizes. From there, the consideration of two materials was sized by utilizing a 1D thermal circuit. This equation follows similarly to equation 28, with the insulation being swapped for a thermal load-bearing material on top of the vehicle. The material selection justifications will be discussed further in section 3.8.2.

The control surfaces (rudders and wings) were sized by extrapolating the design of the X-43 [20] proportionally to the size of the X-68. The leading-edge sizing was followed similarly by scaling from the X-43, however, the shape was justified by the actual X-43 leading-edge development [21].

3 Results and Discussion

3.1 Trajectory

Figure 2 shows the thrust, dynamic pressure, Mach number, and altitude of the booster-vehicle system during the boosted phase of the trajectory. It can be seen that the maximum thrust is below that which the Falcon 1 is able to produce. Moreover, the trajectory was optimized to be as short as possible, reaching two peaks of maximum thrust that are achievable by the booster.

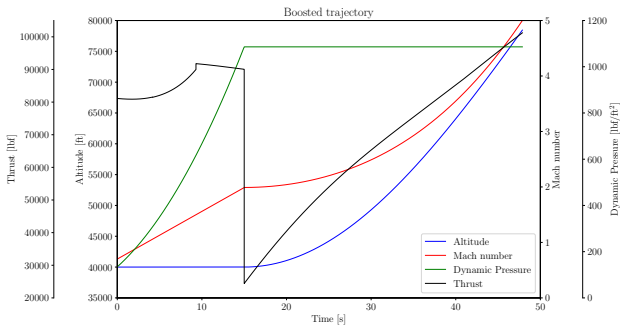


Figure 2: Altitude, Mach number, thrust, and dynamic pressure during the boosted phase of the trajectory. First 15 seconds are at constant altitude and linear acceleration and then constant-q.

Figure 3 plots the flight statistics of the X-68 during the propelled phase of the trajectory. The maximum thrust is achieved at the end of the constant θ climb. As soon as the vehicle starts to reduce the angle, the thrust required starts to decrease. During this part of the flight, the average climbing rate is 131 ft/s, taking 176.6 s to reach the desired Mach number and traveling 245.2 miles. During the remaining part of the propelled flight, the vehicle cruises at Mach 9 and increases the altitude to balance the loss in

weight, climbing at 13.5 ft/s. The total distance traveled by the X-68 is 723 miles and it takes 456.6 s.

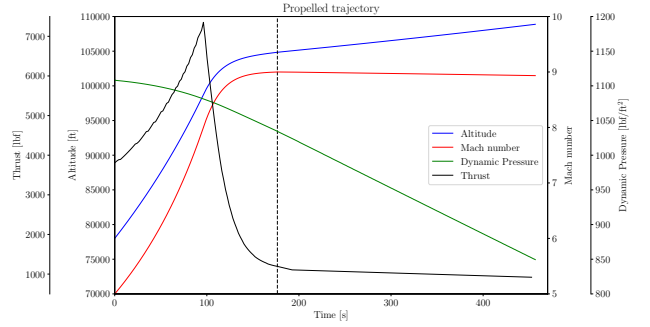


Figure 3: Altitude, Mach number, thrust, and dynamic pressure during the propelled phase of the trajectory. In the first part the vehicle climbs at $\theta = 2^\circ$, after reaching Mach 9 it cruises at constant Mach and balanced flight.

Figure 4 plots the altitude and Mach number of the vehicle after burning all the fuel and gliding down with a weight of 2,866 lb. Different gliding angles were analyzed and it was found that the one that allows the longest distance is $\theta = 0^\circ$. Similar results were achieved by Karlgaard et al. [22], in which the X-43 flight telemetry was analyzed and showed that there is an almost linear decrease of the Mach number with time and a rapid decrease of the altitude toward the end of the flight. After the gliding phase, the vehicle travelled in total 1515 miles in 1326 s.

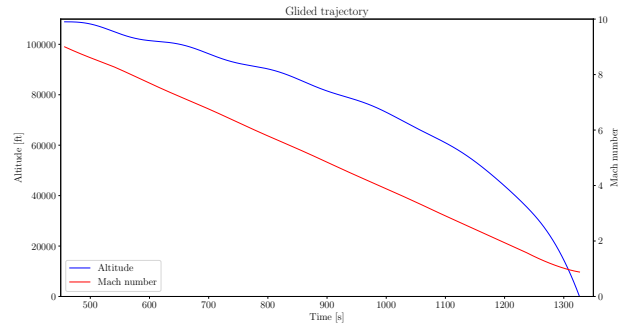


Figure 4: Altitude and Mach number of the vehicle while gliding to the ground.

3.2 Propulsion Cycle

Figure 5 shows the non-dimensional T-s diagram. This diagram is obtained at a nominal compression ratio of 250 and a fuel-flow rate of 2.2 lbm/s and an air flow rate of 39.0 lbm/s. Here, the inefficiencies and entropy gains are shown in clear detail and it is obtained as expected from a scramjet operating in a semi-ideal Brayton cycle.

The compression entropy gain is from the shocks and entropy gain is and temperature rise occur hand-in-hand, implying the shocks are the only source of irreversibility. The combustor analysis being carried out in a 1-D marching manner (Section 2.5.2) hence the entropy rise in great detail is observed here and it is being tracked for every one

of those 0.05” subsections. The nozzle efficiency being assumed to be 0.98 captures any small irreversibilities. These irreversibilities are also captured in the very small but non-zero entropy rise as observed through the nozzle.

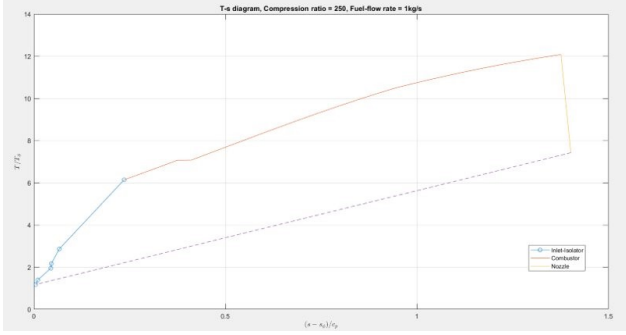


Figure 5: Non-dimensional T-s diagram

Figure 6 shows the parametric cycle analysis. Here, the trade-off between specific fuel consumption and cycle efficiency is observed.

A higher fuel-flow rate, hence a higher fuel-air ratio increases the specific thrust but this is at the cost of overall cycle efficiency, while a higher compression ratio yields a higher efficiency without much loss in specific thrust.

Hence, to meet a certain high thrust requirement, the fuel flow rate can be increased at the cost of efficiency and the compression ratio can also be increased to offset this loss. This is not much of a detriment since a near-max thrust requirement lasts for very little time and the engine can operate at a higher cycle efficiency for most of the flight.

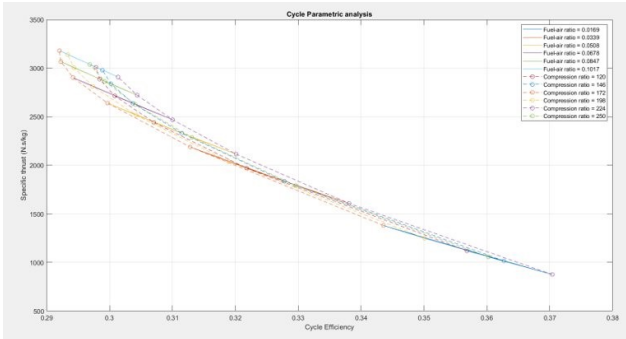


Figure 6: Parametric Cycle Analysis: Specific Fuel Consumption vs. Cycle Efficiency

3.3 Inlet

The first step in determining the final design of the inlet is to solve for the optimal number of turns. This was separated into internal and external turns. Most of the literature and past designs point toward an internal turn number of either one or two. By adjusting the number of turns in the external section along with the number of internal turns the total number of turns was held constant at four. The difference between these two is shown in Table 2.

Based on this information, it was deduced that the two-turn is the best option for internal compression. The total pressure recovery, as well as the temperature increase, are

Turns	$P_{02}/P_{0\infty}$	T_2/T_∞	M_2
1	0.4313	4.7662	3.6116
2	0.5761	4.0792	4.0103

Table 2: Internal Turns

both lower. While the inlet does not slow down the flow as much, the other two values are more critical to the efficiency and structural capabilities of the airframe.

To determine the number of external turns the outputs are compared using simple weighted metrics based on perceived importance. There are 6 total metrics with a total weight of 100%: temperature gain (10%), range of pressure increase (5%), pressure recovery (20%), length (25%), isolator entrance Mach (15%), and isolator/combustor height (25%). The geometry values were held to be more critical in this analysis because the airflow characteristics all met the requirements. Figure 7 shows diminishing returns began to be realized after 4 turns.

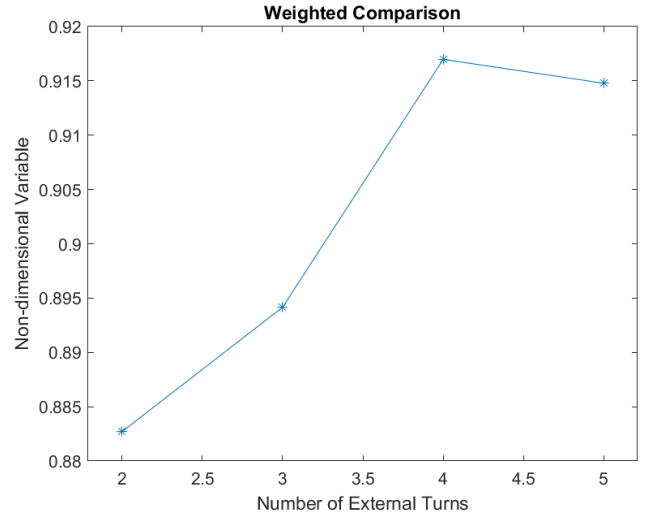


Figure 7: Weighted Analysis

According to the work by Smart, limiting the pressure increase is beneficial to limiting the losses created by real gas effects. [5] While more work needs to be done to determine the minimum pressure that can be input in the algorithm. For this preliminary design, the pressure ratio was set to be 35.

The design that was implemented had inputs of a Mach range of 7 to 9, a pressure ratio of 35, external turns of 4, and internal turns of 2. To adjust for the necessary size of the combustor the inlet was scaled so the isolator height is equal to 1.5”. The design that was developed and the location of each of the points is included in Figure 8. As previously discussed in section 2.3 the inlet was integrated into the lower portion of the airframe. This can be seen in Figure 17

3.4 Isolator

The isolator length-to-height ratio was determined to be approximately 2.26. This combined with the isolator height

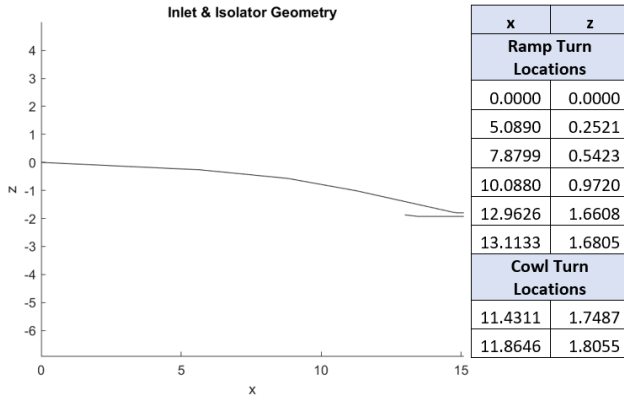


Figure 8: 2D Design and Points of Interest

of 1.5" that was determined in section 3.4 results in an isolator length of 3.39". Analysis can then be done with the combined inlet/isolator results in the total ratios that are included in Figure 9. The Mach values at each part of the inlet and isolator are included in Figure 10.

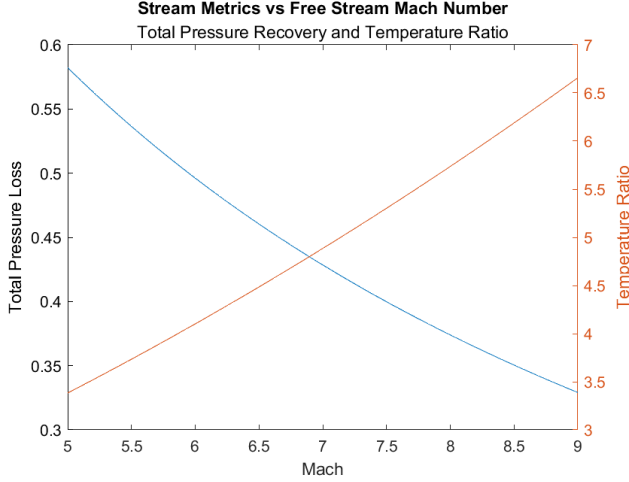


Figure 9: Total Pressure Recovery and Temperature

Figure 9 shows that the total pressure loss meets the requirements set by the MIL-E-5007D [7]. The lowest total pressure recovery is well over the limit of 0.1. Figure 10 shows that Mach at the entrance to the combustor is reduced to below Mach 2.8 at all flight conditions but also stays high enough at Mach 5 that the combustor can avoid thermal choking.

3.5 Combustor

Using the combustor model developed, the combustor geometry and fuel flow rates were determined. A basic CAD model of this geometry is shown in Figure 11. To achieve the desired mixing and combustion efficiencies, half of the main fuel flow rate is injected in the upstream normal port injectors, and the other half is injected in the ramp hypermixers. At the cruise condition, the total fuel flow rate is 2.2 lbm/s, with 0.1 lbm/s of that being supplied to the cavity pilot flame and 1.05 lbm/s to each main injection point. All the injection ports were sized based on providing these

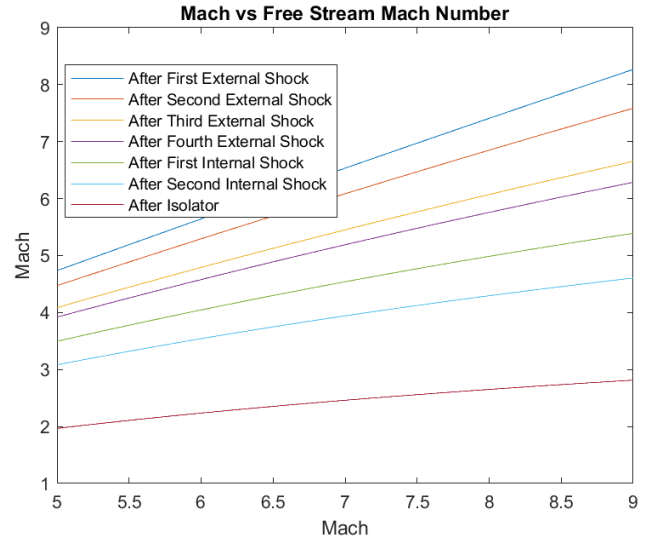


Figure 10: Mach Values Across Inlet Differing Flight Machs

flow rates at 200 psia and -10 °F. To achieve adequate mixing and performance, the combustor runs fuel-rich at the cruise condition with a global equivalence ratio of 1.54.

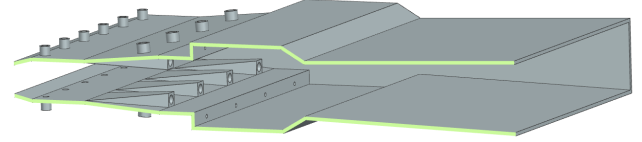


Figure 11: Full CAD model of combustor.

For the upstream normal port injectors, it was decided to have 12 sonic ports that are 0.29" in diameter, giving even mixing across the combustor width. This section was chosen to be a constant-area duct to facilitate rapid heat release. Equation 11 was used to ensure the duct was long enough for the fuel to reach the combustor centerline, as shown in Figure 12. This resulted in a length of 7.5".

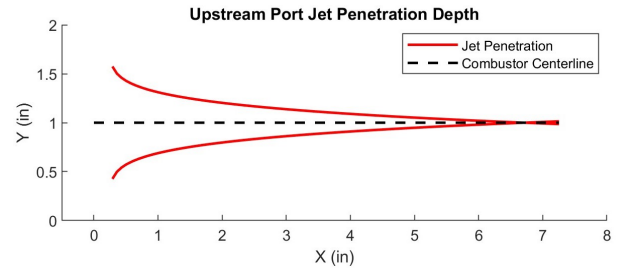


Figure 12: Upstream normal port injector jet penetration.

For the ramp hypermixers, it was determined to have 8 swept ramps, each with a sonic port that is 0.35" in diameter. This section also has a constant flow area to promote heat release. The combustor wall expands through this section to maintain a constant area, offsetting the area consumed by the protruding ramps. Equation 15 was used to size the length of the duct following the ramps to 3.25", ensuring it is long enough for the mixing layer to reach the

centerline before the cavity flameholder, as demonstrated in Figure 13.

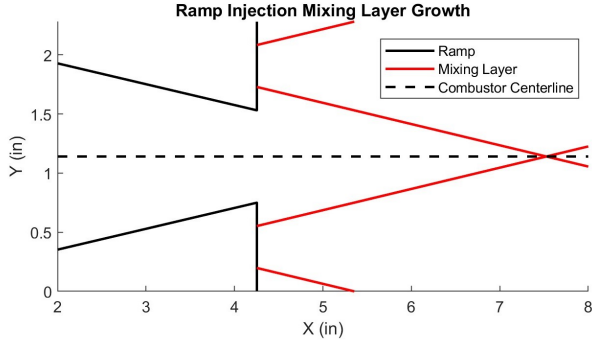


Figure 13: Ramp hypermixer mixing layer growth.

The cavity flameholder was chosen to have a depth of 0.75", a length of 6.25", and a 30° aft ramp. This gives a L/D of 8.33 and classifies it as an "open" cavity. This enhances flame stability and decreases drag losses [23]. Since the pilot fuel is not being injected into a supersonic cross-flow, its momentum does not need to be as high as the other injectors. As such, the pilot fuel is injected at a Mach number of 0.5 through 8, 0.13"-diameter ports.

To reach the desired combustion efficiency of 80%, the diverging duct is 12" long. To prevent thermal choking at the low freestream Mach numbers present during the initial trajectory, the duct has a 2° expansion.

With this geometry and the fuel flow rates stated above, the mixing and combustion efficiency profiles shown in Figure 14 were found. It can be seen that the 80% combustion efficiency goal is achieved, and the mixing efficiency reaches premixed conditions at the entrance to the cavity flameholder.

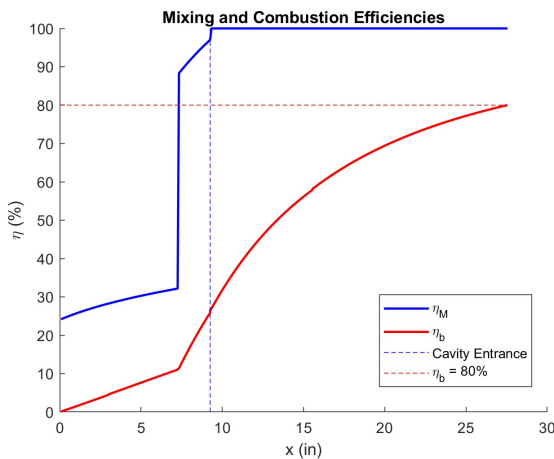


Figure 14: Combustor mixing and combustion efficiencies.

3.6 Nozzle

Using the ideal MOC contour analysis discussed in Section 2.6.1, the X-68's nozzle was designed. To meet the full MOC contour, the nozzle expansion ramp is 75" long with

a height of 19.5", and the flap is 20.5" long. In addition to providing the nominal thrust at cruise conditions, the nozzle flap enables variable geometry for thrust modulation. The flap is connected to the combustor via a hinge, allowing for actuators to open or close it to change the flow area. While changing flow area will change the thrust produced by the nozzle, the flow no longer follows the ideal MOC contour, and thrust efficiency is decreased.

At the cruise conditions, the nozzle accepts combustor exit flow at a Mach number of 2.2 and exhausts it at a Mach number of 3.8, producing just over 1000 lbf. As seen in Figure 3, there is a large peak in thrust of over 7000 lbf near the end of the initial climb. This thrust can be achieved by opening up the nozzle flap to 15° and increasing the injection pressure to ramp the fuel flow rate up to 7.7 lbm/s through this peak.

3.7 Thermal Management

Figures 15 and 16 illustrate the temperature trends in the combustor and nozzle, and the leading edge, respectively. The internal wall temperature of the combustor is made of molybdenum and is successfully maintained at 2600°F, a viable temperature for maintaining yield strength. The actively cooled nozzle operates at lower temperatures, allowing the use of titanium instead of molybdenum. This substitution significantly reduces weight. To find the convective heat transfer in the leading edge, the Bartz correlation is replaced by the Dittus Boelter correlation for a flat plate. For this part, it was considered a constant temperature of 6800°F (stagnation temperature on the leading edge at Mach 9). Following the cooling process, the wall temperature of the leading edge was successfully lowered to 5500°F, a sustainable level for the reinforced carbon-carbon (RCC) panels.

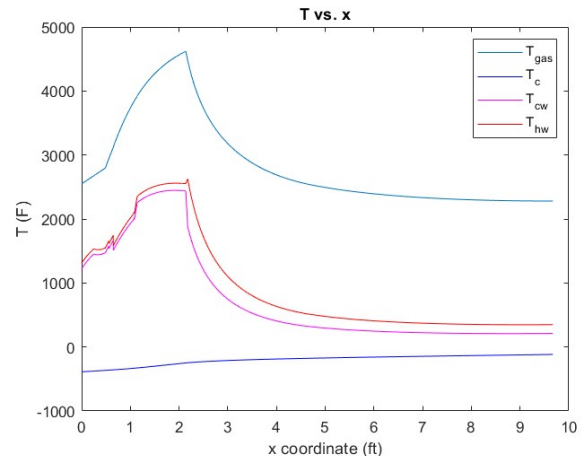


Figure 15: Combustor and nozzle temperature profile.

3.8 Mechanical Design

3.8.1 Tanks

The primary cryogenic hydrogen propellant tank utilizes Aluminum-Lithium 2195 alloy for its material construction.

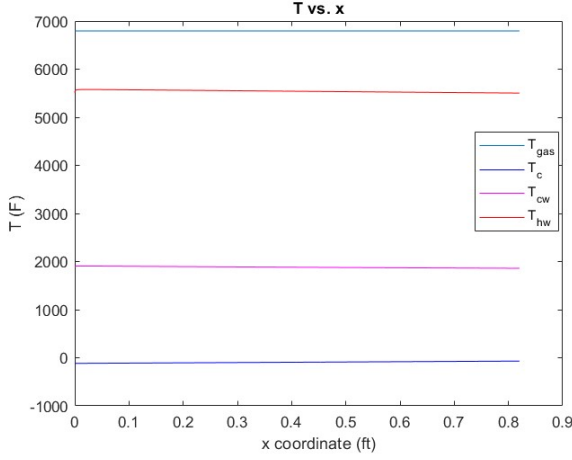


Figure 16: Leading edge temperature profile.

Al-Li 2195 offers an optimal combination of low density and high mechanical strength retention in cryogenic hydrogen environments [24]. The cylindrical tank dimensions were optimized to roughly 5 m in length, 0.6 m in radius, and 1.5 mm in thickness.

Spray-on foam insulation (SOFI) was selected for the hydrogen tank based on prior NASA use on the Space Shuttle external tanks. It couples with the analysis well because it provides low conductivity ($<0.1 \text{ W/mK}$) and minimizes weight. SOFI provides the optimal balance of permeability, molecular weight, and handling properties with flight heritage [25]. The optimal thickness chosen was 50 mm, limiting additional boil-off propellant to under 50 kg.

To provide the driving gas for propellant tank pressurization, a lightweight composite overwrapped pressure vessel (COPV) contained the helium storage supply. By using a Ti-6Al-4V metallicity lined tank with a carbon fiber reinforced plastic overwrap, the helium tank could be pressurized highly with minimal weight addition [26].

Cryogenic hydrogen tanks and distribution system weights were projected based on historical mass growth trends documented by NASA [19]. This allowed for an estimate to be formed for the remaining fluid system, sized to be at about 150 lbf. The mass breakdown for the entire tank and fluid system, including propellant and helium masses, can be seen in table 4 in Appendix E, with the total mass of this system also being reported in table 3.

3.8.2 Vehicle Structure

RCC forms the blunt leading edge, the underbody of the inlet, and the panels on the entirety of the aircraft. RCC provides the best combination of high-temperature capability, low coefficient of thermal expansion, and marginal increased growth under thermal load [27]. At 4.8 mm thickness, the leading edge resists thermal loads yet maintains minimal mass.

The primary load-bearing structure and the isolator use Inconel 625 nickel alloy. Inconel offers the best ambient temperature tensile properties among feasible nickel alloys, in a weldable form necessary for intricate main frame joints

[28]. The structure withstands the maximum dynamic pressure and other aerodynamic loads, while the RCC panels lay bolted on top of it. The control surfaces of the vehicle contain a similar split of RCC and Inconel. The weights of the general structures can be seen in table 3. The total weight of 3505.63 lbf is verified as below the maximum requirement. For trajectory mass matching purposes, this design can reach 4000 lbf by increasing margins on thicknesses and insulation, which helps the performance of the vehicle.

Figure 17 shows the general shape of the X-68. The aeroshell surface is designed to have smooth contours to manage shock waves and boundary layer transitions. The blunt leading edge is inspired by the X-43, which was proven to help deal with intense shock wave interactions at high hypersonic speeds [29].

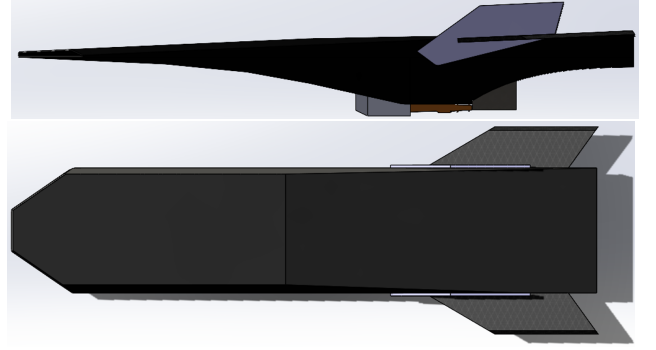


Figure 17: Component integrated vehicle CAD.

Component/System	Design Mass (kg)	Design Mass (lbf)
Airframe/Aeroshell (including inlet)	750	1653.47
Combustor & Nozzle	54.43	120
Wing & Rudder	122.47	270
Tanks & Fluid System	629.9	1382.16
Avionics	36.29	80
Total	1590.09	3505.63

Table 3: Total Vehicle Mass Breakdown

4 Conclusions

This comprehensive analysis and vehicle synthesis meets or exceeds all mission requirements set forth for the X-68 Velociraptor. To meet the design requirements, the X-68 utilizes a hydrogen-fueled scramjet engine integrated into the vehicle's underbody structure. Utilizing only existing materials to have a take-off mass of 3506 lbf, the X-68 launches from the B-52 and is optimized to cruise at Mach 9 and 104,843 feet, providing a range of over 700 miles during its propelled flight. The successful design of major subsystems and their integration establishes viability for continued scramjet technology development. Future work should focus on validation through higher-fidelity numerical modeling and ground testing of subscale experimental hardware.

References

- [1] Corin Segal. *The Scramjet Engine Processes and Characteristics*. Cambridge University Press, New York, 2009.
- [2] William H. Heiser and David T. Pratt. *Hypersonic Airbreathing Propulsion*. AIAA, Washington D.C., 1994.
- [3] Flight separation mechanisms. *NASA space vehicle design criteria (structures)*, 1970.
- [4] Àlex Navó and Josep M Bergada. Aerodynamic study of the nasa’s x-43a hypersonic aircraft. *Applied Sciences*, 10(22):8211, 2020.
- [5] Micheal K. Smart. Scramjet Inlets. *NATO OTAN*, 2010.
- [6] Philip Harsha, Lowell Keel, Anthony Castrogiovanni, and Robert Sherrill. X-43A Vehicle Design and Manufacture. In *AIAA/CIRA 13th International Space Planes and Hypersonics Systems and Technologies Conference*, Capua, Italy, May 2005. American Institute of Aeronautics and Astronautics.
- [7] Military Specifications: Engines, Aircraft, Turbojets, and Turbofans, General Specifications for, 1973.
- [8] Sean Torrez, James Driscoll, Derek Dalle, and Matthew Fotia. Preliminary Design Methodology for Hypersonic Engine Flowpaths. In *16th AIAA/DLR/DGLR International Space Planes and Hypersonic Systems and Technologies Conference*, Bremen, Germany, October 2009. American Institute of Aeronautics and Astronautics.
- [9] Jose A. Medina, Harinkumar Patel, and Bernd Chudoba. Inlet Sizing of Hypersonic Vehicles for Conceptual Design. In *ASCEND 2021*, Las Vegas, Nevada & Virtual, November 2021. American Institute of Aeronautics and Astronautics.
- [10] X. Song et al. Mixing and combustion characteristics in a cavity-based supersonic combustor with different injection schemes. *Acta Astronautica*, 159:584–592, 2019.
- [11] Ascher H. Shapiro and W. R. Hawthorne. The mechanics and thermodynamics of steady one-dimensional gas flow. *Journal of Applied Mechanics*, 14(4):A317–A336, 1947.
- [12] G. Ebenhoc K. Rued and H. Mark. Thermal management of propulsion systems in hypersonic vehicles. *30th Aerospace Sciences Meeting Exhibit*, 1992.
- [13] Bergman Incropera, Dewitt and Lavine. *Fundamentals of Heat and Mass Transfer*. John Wiley Sons, Inc., sixth edition, 2001.
- [14] Ten See Wang and Van Luong. Hot gas side and coolant side heat transfer in liquid rocket engine combustors. *JOURNAL OF THERMOPHYSICS AND HEAT TRANSFER*, 8(3), 1994.
- [15] D. R. Bartz. A simple equation for rapid estimation of rocket nozzle convective heat transfer coefficients. Technical report, Jet Propulsion Laboratory, 1957.
- [16] Morris W. Rubesin Jackson R. Stalder and Thorval Tendeland. A determination of the laminar, transitional, and turbulent boundary layer temperature recovery factors on a flat plate in supersonic flow. Technical report, Ames Aeronautical Laboratory, 1950.
- [17] Th. Von Karman. Turbulence and skin friction. *Journal of the Aeronautical Sciences*, 1(1), 1934.
- [18] Raymond J. Roark, Warren C. Young, Richard G. Budynas, and Ali M. Sadegh. *Roark’s formulas for stress and strain*. McGraw-Hill, New York, 8th ed edition, 2012. OCLC: ocn769455976.
- [19] Alok K. Majumdar, Andre LeClair, and Ali Hedayat. Numerical Modeling of Pressurization of Cryogenic Propellant Tank for Integrated Vehicle Fluid System. In *52nd AIAA/SAE/ASEE Joint Propulsion Conference*, Salt Lake City, UT, July 2016. American Institute of Aeronautics and Astronautics.
- [20] Laurie Marshall, Griffin Corpening, and Robert Sherrill. A Chief Engineer’s View of the NASA X-43A Scramjet Flight Test. In *AIAA/CIRA 13th International Space Planes and Hypersonics Systems and Technologies Conference*, Capua, Italy, May 2005. American Institute of Aeronautics and Astronautics.
- [21] C. W. Ohlhorst et al. Development of X-43A Mach 10 Leading Edges. In *56th International Astronautical Congress of the International Astronautical Federation, the International Academy of Astronautics, and the International Institute of Space Law*, Fukuoka, Japan, October 2005. AIAA.
- [22] Christopher Karlgaard, John Martin, Paul Tartabini, and Mark Thornblom. Hyper-x mach 10 trajectory reconstruction. In *AIAA Atmospheric Flight Mechanics Conference and Exhibit*, page 5920, 2005.
- [23] M. R. Gruber, R. A. Baurle, T. Mathur, and K. Y. Hsu. Fundamental studies of cavity-based flameholder concepts for supersonic combustors. *Journal of Propulsion and Power*, 17(1):146–153, 2001.
- [24] Richard Martukanitz and Jan R. A fundamental study of laser beam welding aluminum-lithium alloy 2195 for cryogenic tank applications. 10 1996.
- [25] J.E. Fesmire, B.E. Coffman, B.J. Meneghelli, and K.W. Heckle. Spray-on foam insulations for launch vehicle cryogenic tanks. *Cryogenics*, 52(4):251–261, 2012. 2011 Space Cryogenics Workshop.
- [26] P. B. McLaughlan, Scott C. Forth, and Lorie Grimes-Ledesma. Composite overwrapped pressure vessels, a primer. 2011.
- [27] Donald M. Curry, Vuong T. Pham, Ignacio Norman, and Dennis C. Chao. Oxidation of Hypervelocity Impacted Reinforced Carbon-Carbon. *Journal of Spacecraft and Rockets*, 37(3):310–317, May 2000.
- [28] A H Knoll and J W Clark. Structural efficiency of materials at elevated temperatures. report no. 12-57-38a. 7 1958.
- [29] Adam Peters, Zhang Dajie, Samuel Chen, Catherine Ott, Corey Oses, Stefano Curtarolo, Ian McCue, Tresa Pollock, and Suhas Eswarappa Prameela. Materials design for hypersonics. 09 2023.

A Jet Penetration Correlation Coefficients [1]

$$\begin{aligned} A &= 1.05M_a - 0.192 \\ B &= -0.0803M_a + 0.615 \\ C &= -2.34/M_a \\ E &= 0.406M_a^{-0.823} \\ F &= -0.067M_a + 0.325 \\ G &= -0.0251 \end{aligned}$$

In these coefficients, M_a is the Mach number of the air at the entrance of the combustor.

B Generalized 1-D Flow Analysis ODEs [11]

$$\begin{aligned} \frac{dM^2}{M^2} &= -\frac{2(1 + \frac{\gamma-1}{2}M^2)}{1-M^2} \frac{dA}{A} + \frac{1+\gamma M^2}{1-M^2} \frac{dH}{c_p T} + \\ &\frac{2(1+\gamma M^2)(1 + \frac{\gamma-1}{2}M^2)}{1-M^2} \frac{d\dot{m}}{\dot{m}} - \frac{1+\gamma M^2}{1-M^2} \frac{dMW}{MW} - \frac{d\gamma}{\gamma} \end{aligned} \quad (30)$$

$$\begin{aligned} \frac{dP}{P} &= \frac{\gamma M}{1-M^2} \frac{dA}{A} - \frac{\gamma M^2}{1-M^2} \frac{dH}{c_p T} - \\ &\frac{2\gamma M^2(1 + \frac{\gamma-1}{2}M^2)}{1-M^2} \frac{d\dot{m}}{\dot{m}} + \frac{\gamma M^2}{1-M^2} \frac{dMW}{MW} \end{aligned} \quad (31)$$

In these ODEs, M is Mach number, P is static pressure, γ is ratio of specific heats, A is flow area, H is static enthalpy, c_p is specific heat, T is static temperature, \dot{m} is mass flow rate, and MW is molecular weight.

C Thermal Analysis Equations

The following is the Bartz correlation [15]

$$h_g = \frac{(0.026)}{D_*^{0.2}} \left(\frac{\mu^{0.2} c_p}{P_r^{0.6}} \right) \left(\frac{P_c g}{c^*} \right)^{0.8} \left(\frac{D_*}{r_c} \right)^{0.1} \left(\frac{A_*}{A} \right)^{0.9} \sigma \quad (32)$$

$$\sigma = \frac{1}{\left(\frac{1}{2} \frac{T_{hvw}}{T_0} \left(1 + \frac{\gamma-1}{2} M^2 \right) + \frac{1}{2} \right)^{(0.8 - \frac{W}{5})} \left(1 + \frac{\gamma-1}{2} M^2 \right)^{\frac{W}{5}}} \quad (33)$$

Nusselt number equation for a tube with hydraulic diameter D_h [14]

$$Nu = \frac{\frac{f}{8}(Re_{D_h} - 1000)Pr}{1 + 12.7\sqrt{\frac{f}{8}}\left(Pr^{\frac{2}{3}} - 1\right)} \quad (34)$$

Von Kármán equation [17]

$$\frac{1}{\sqrt{f}} = 4 \log_{10}(Re_{D_h} \sqrt{f}) - 0.4 \quad (35)$$

Dittus-Boelter correlation [13].

$$Nu_{D_h} = \frac{h_c D_h}{k_f} \quad (36)$$

Darcy-Weisbach equation:

$$\Delta P = \frac{1}{2} \frac{f}{D_h} \rho_{H_2} U^2 dx \quad (37)$$

D Generalized P&ID Diagram

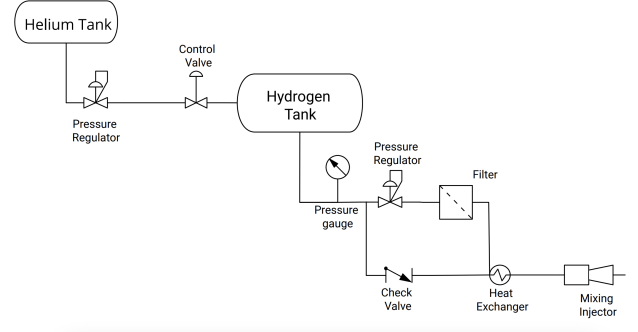


Figure 18: Simple P&ID representing the tank fluid system flow path toward the injector and combustor.

E Tank and Fluid System Mass Breakdown

Component/System	Design Mass (kg)	Design Mass (lbf)
Required Propellant	400	881.85
Propellant Tank	74.1	163.36
Insulation	22.6	49.82
Boil-off Propellant	48.7	107.37
Helium	2.7	5.95
Helium Tank	10.8	23.81
Fluid System	68.0	150
Total	626.9	1382.16

Table 4: Total Tank and Fluid System Mass